A&A 549, A62 (2013)
DOI: 10.1051/0004-6361/201118556

Astronomy & Astrophysics

Multi-epoch high-resolution spectroscopy of SN 2011fe

Linking the progenitor to its environment⋆

F. Patat[1], M. A. Cordiner[2], N. L. J. Cox[3], R. I. Anderson[4], A. Harutyunyan[5], R. Kotak[6], L. Palaversa[4], V. Stanishev[7], L. Tomasella[8], S. Benetti[9], A. Goobar[10], A. Pastorello[9], and J. Sollerman[10]

[1] European Organization for Astronomical Research in the Southern Hemisphere (ESO), Karl-Schwarzschild-Str. 2, 85748, Garching b. München, Germany
e-mail: fpatat@eso.org
[2] Astrochemistry Laboratory and the Goddard Center for Astrobiology, Mailstop 691, NASA Goddard Space Flight Center, 8800 Greenbelt Road, Greenbelt, MD 20770, USA
[3] Instituut voor Sterrenkunde, KU Leuven, Celestijnenlaan 200 D, 3001 Leuven, Belgium
[4] Observatoire de Genève, Université de Genève, 51 Ch. des Maillettes, 1290 Sauverny, Switzerland
[5] Fundación Galileo Galilei - Telescopio Nazionale Galileo, Rambla José Ana Fernández Pérez 7, 38712 Breña Baja, TF, Spain
[6] Astrophysics Research Center, School of Mathematics and Physics, Queens University Belfast, Belfast, BT7 1NN, UK
[7] CENTRA – Centro Multidisciplinar de Astrofísica, Instituto Superior Técnico, Av. Rovisco Pais 1, 1049-001 Lisbon, Portugal
[8] INAF, Osservatorio Astronomico di Padova, via dell'Osservatorio 8, 36012 Asiago (VI), Italy
[9] INAF, Osservatorio Astronomico di Padova, v. Osservatorio n. 5, 35122 Padua, Italy
[10] Albanova University Center, Department of Physics, Stockholm University Roslagstullsbacken 21, 106 91 Stockholm, Sweden

Received 1 December 2011 / Accepted 12 July 2012

ABSTRACT

Aims. The nearby Type Ia supernova (SN) 2011fe has provided an unprecedented opportunity for deriving some of the properties of its progenitor. This work provides additional and independent information on the circumstellar environment in which the explosion took place.
Methods. We obtained high-resolution spectroscopy of SN 2011fe for 12 epochs, from 8 to 86 days after the estimated date of explosion, testing in particular the time evolution of Ca II and Na I.
Results. Three main absorption systems are identified from Ca II and Na I, one associated to the Milky Way, one probably arising within a high-velocity cloud, and one most likely associated to the halo of M101. The total (Galactic and host galaxy) reddening, deduced from the integrated equivalent widths (EW) of the Na I lines, is $E_{B-V} \lesssim 0.05$ mag. The host galaxy absorption is dominated by a component detected at the same velocity measured from the 21-cm H I line at the projected SN position ($\sim$180 km s^{-1}). During the $\sim$3 months covered by our observations its EW peak-to-peak variation is 15.6 ± 6.5 mÅ. This small and marginally significant change is shown to be compatible with the geometric effects produced by the rapid SN photosphere expansion coupled to the patchy fractal structure of the interstellar medium (ISM). The observed behavior is fully consistent with ISM properties similar to those derived for our own Galaxy, with evidences for structures on scales $\lesssim$100 AU.
Conclusions. SN 2011fe appears to be surrounded by a "clean" environment. The lack of blueshifted, time-variable absorption features is fully consistent with the progenitor being a binary system with a main-sequence, or even another degenerate star.

Key words. supernovae: general – supernovae: individual: SN2011fe – ISM: general – dust, extinction – ISM: clouds

1. Introduction

Since the introduction of the accreting white dwarf (WD) scenario (Wheelan & Iben 1973), the question about the nature of the progenitor systems of Type Ia supernovae (hereafter SN Ia) has become more and more pressing (see Patat 2011, for a general review on the subject). One of the most well beaten tracks for obtaining information on the progenitor system has been the search for imprints of circumstellar material (CSM) lost by the system prior to the explosion. Notwithstanding the extensive attempts undertaken to detect such material, as of today no signs of it have been found in Branch-normal events in the form of optical (Lundqvist 2003, 2005; Mattila et al. 2005), radio (Panagia et al. 2006, Chomiuk et al. 2011) and UV/X-ray emission (Immler et al. 2006). Similarly, no evidence for the explosion effects on the companion (e.g. collision and/or envelope stripping) was found so far (Hayden et al. 2010; Bianco et al. 2011; Leonard 2007).

These non-detections were generally interpreted as favoring progenitor systems where the donor is either a main sequence (MS) star, or another degenerate object. However, it is only with the advent of SN 2011fe that very stringent constraints could be placed on the exploding star and its companion. This SN Ia was discovered by the Palomar Transient Factory in the nearby, face-on galaxy M101, less than one day after the explosion (Nugent et al. 2011a,b). The detailed optical and UV studies made possible by the very early detection and the relatively small distance led to two important conclusions: i) the exploding star

⋆ Based on observations collected at the Mercator telescope, Telescopio Nazionale Galileo, Nordic Optical Telescope at Roque de los Muchachos, La Palma (Spain), and at the 1.82 m Copernico telescope on Mt. Ekar (Asiago, Italy).

Table 1. Log of the observations.

Date	UT (start)	JD (start)	Phase (days)*	Epoch (days)**	Airmass (start)	Exposure (s)	Instrument	Hel. correction (km s^{-1})
2011-08-31	20:39	24 55 805.357	−10	8.2	1.64	1800	FIES	−4.19
2011-09-03	20:20	24 55 808.344	−7	11.2	1.52	3600	SARG	−3.46
2011-09-07	20:20	24 55 812.340	−3	15.1	1.58	1800	HERMES	−2.47
2011-09-13	19:23	24 55 818.308	+3	21.1	1.60	4200	AES	−0.94
2011-09-13	20:16	24 55 818.342	+3	21.1	1.72	1350	HERMES	−0.96
2011-09-14	18:57	24 55 819.290	+4	22.1	1.50	3600	AES	−0.69
2011-09-21	18:59	24 55 826.291	+11	29.1	1.63	5400	AES	+1.09
2011-09-22	18:40	24 55 827.278	+12	30.1	1.56	9000	AES	+1.35
2011-09-29	20:47	24 55 834.363	+19	37.2	2.63	2700	FIES	+3.10
2011-10-18	17:54	24 55 853.246	+38	56.1	1.84	7200	AES	+7.68
2011-11-15	16:52	24 55 881.203	+66	84.0	2.80	4800	AES	+12.86
2011-11-18	01:28	24 55 883.561	+68	86.4	2.65	12600	AES	+13.52
2011-11-18	05:05	24 55 883.710	+68	86.5	2.92	4800	SARG	+13.55

Notes. * Phases from B maximum were computed assuming a rise time of 18.3 days (Röpke et al. 2012). ** Epochs were computed from the estimated explosion time (JD = 2 455 797.196; Nugent et al. 2011c).

must be a compact body (a C-O WD is most favored); and ii) systems with Roche-lobe overflowing giants and MS stars as companions are excluded (Li et al. 2011; Nugent et al. 2011c; Brown et al. 2012; Liu et al. 2012; Bloom et al. 2011). The very stringent limits on the mass loss rate set by radio and X-ray observations point in the same direction (Horesh et al. 2012; Chomiuk et al. 2012; Margutti et al. 2012).

After studying an object whose progenitor system is reasonably well known, we can now ask ourselves a new question. Would we recognize similar systems in other SN Ia, whose distance and discovery time do not allow the close, multi-wavelength scrutiny that was possible for SN 2011fe? The key problem here is that one needs to consider the largest possible number of observables, because SN Ia coming from different channels may display similar spectra and light curves.

In this article we focus on the properties of the circumstellar environment. For this purpose, and following previous studies (e.g. Patat et al. 2007a; Simon et al. 2009), we obtained multi-epoch, high-resolution, optical spectroscopy of SN 2011fe covering the first three months of its evolution. The paper, reporting the results of this campaign, is structured as follows. In Sect. 2 we give an account of the observations and data reduction. Section 3 describes the detection of narrow absorption features, whereas Sect. 4 discusses the implications on the extinction suffered by the SN. In Sect. 5 we illustrate the properties of the intervening gas as derived from Voigt profile fittings, and we study their behavior as a function of time. The results of this study in connection to the progenitor's nature are finally discussed in Sect. 6, which also summarizes our conclusions.

2. Observations and data reduction

We obtained high-resolution spectroscopy of SN 2011fe for 12 epochs, ranging from 8 to 86 days after the estimated date of explosion (JD = 2 455 797.2; Nugent et al. 2011c). The observing log is presented in Table 1, which includes exposure times, phase from maximum light, epoch from explosion, airmass, and heliocentric correction. Phases were computed by adopting a rise time of 18.3 days (Röpke et al. 2012). The observations were carried out with four different instrumental setups. These are summarized in Table 2 and are detailed in the next subsections.

Table 2. Instrumental setups.

ID	Site	Telescope	Res. power	Disp. (Å/pixel)	Range (Å)
AES	Asiago	1.8-m	18 000	0.126	3800–7500
FIES	La Palma	2.6-m	48 000	0.036	3650–7350
HERMES	La Palma	1.2-m	82 000	0.016	3770–9000
SARG	La Palma	3.5-m	66 000	0.021	4600–6150

2.1. Asiago Echelle Spectrograph

Seven spectra of SN 2011fe were obtained with the REOSC Asiago Echelle Spectrograph (hereafter AES) that is attached to the 1.82 m telescope on Mt. Ekar (Asiago, Italy). The spectrograph is equipped with an an E2V CCD42-40 AIMO, back-illuminated detector (2048 × 2048 pixel, 13.5 μm in size). A 2″ slit was used, with a fixed east-west orientation, yielding a resolving power $R = \lambda/\Delta\lambda \sim 18\,000$. The wavelength range covered by the spectra is 3780–7620 Å. The data reduction was performed with tasks within the IRAF[1] `ECHELLE` package following the standard procedures. All images were first overscan-corrected and trimmed. A normalized flat-field image was then derived from observations of a halogen lamp and was used to flat field the science exposures. Next, each spectral order was traced and the spectra were extracted with the optimum extraction algorithm of Horne (1986), which simultaneously subtracts the scattered light. The transformation from pixels to wavelength was derived from observations of a thorium-argon arc-lamp.

2.2. FIES

Two spectra (Aug. 31 and Sep. 29, 2011) were obtained with the fiber-fed (1.3″) echelle spectrograph (FIES[2]) mounted at the Nordic Optical Telescope (NOT) on La Palma (Spain). We used the medium-resolution fiber, which provides a resolving power $R \sim 48\,000$ and a continuous spectral coverage from 3700 to

[1] IRAF is distributed by the National Optical Astronomy Observatories, which are operated by the Association of Universities for Research in Astronomy, under contract with the National Science Foundation.

[2] http://www.not.iac.es/instruments/fies/

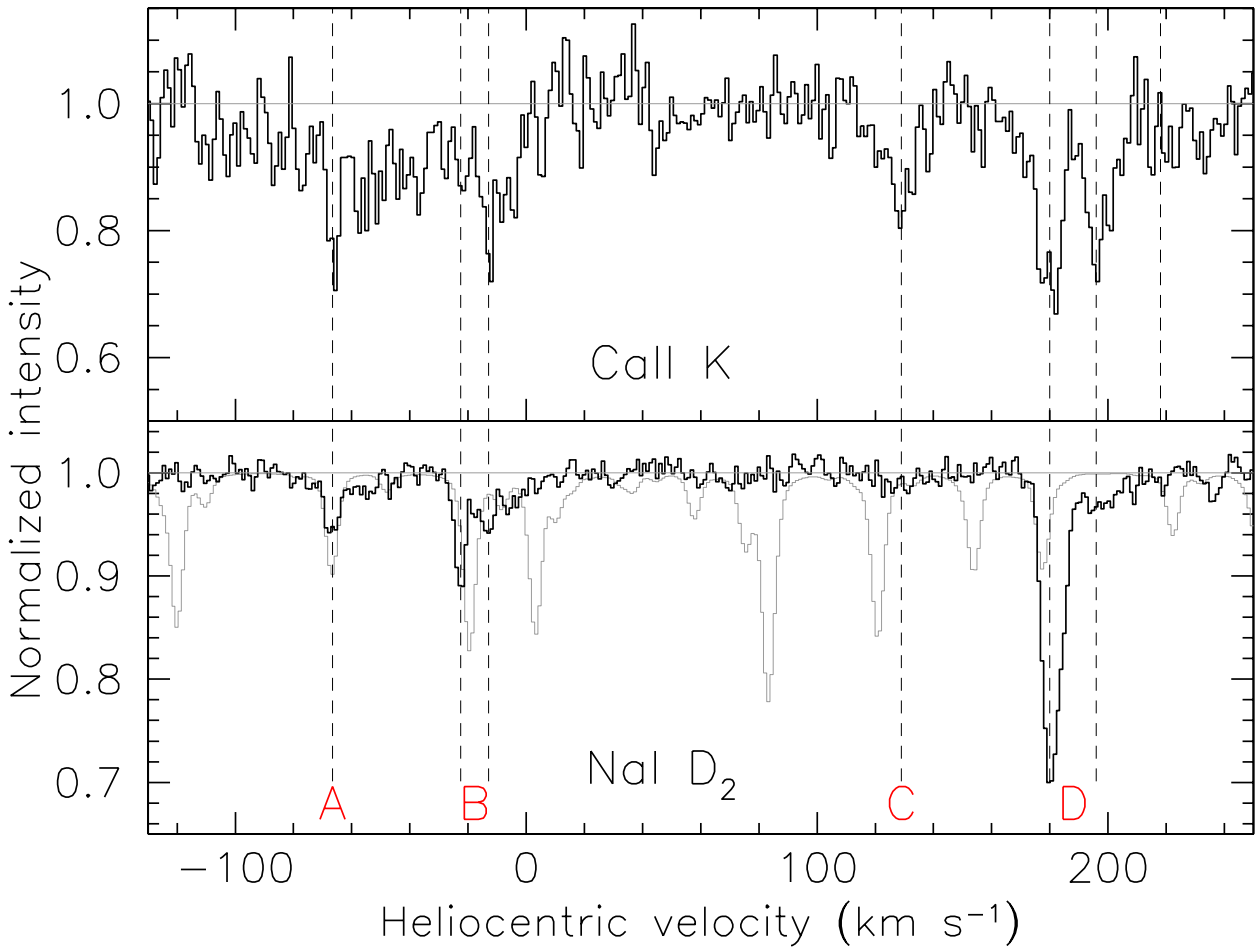

Fig. 1. Narrow absorption components toward SN 2011fe for Ca II K (*upper panel*; day 21) and Na I D_2 (*lower panel*; day 11.2). Main absorption features are marked by vertical dashed lines.

7300 Å in a single exposure. Data were reduced using standard IRAF tasks, as outlined in the previous section.

2.3. HERMES

Two spectra (Sep. 7 and 13, 2011) were obtained with the High Efficiency and Resolution Mercator Echelle Spectrograph (HERMES; Raskin et al. 2011), mounted on the Mercator 1.2 m telescope in La Palma. HERMES is a high-resolution fiber-fed (2.5″) echelle spectrograph offering spectral resolution of $R \sim 80\,000$, and full spectral coverage from 3770 to 9000 Å in a single exposure. Data were processed with an automated data reduction pipeline that includes bias correction from the prescan region on the CCD, flat-field correction via halogen lamps, wavelength calibration through Th-Ar reference spectra, cosmic clipping, and background modelization.

2.4. SARG

Two spectra (Sep. 3, and Nov. 18, 2011) were obtained with the Spettrografo Alta Risoluzione Galileo (SARG; Gratton et al. 2001), mounted at the 3.5 m Telescopio Nazionale Galileo (TNG) in La Palma. SARG is a cross-dispersed echelle spectrograph that provides spectral resolution ranging from $R = 29\,000$ up to $R = 164\,000$. For our observations we used the cross-disperser #3 grism, a GG455 order-sorting filter, and slit #2 (0.8″ × 5.3″). This setup yields $R \sim 66\,000$ and a wavelength range 4600–6150 Å. The data reduction was performed using standard IRAF tasks, as outlined in Sect. 2.1. The removal of telluric absorption features was performed by means of synthetic atmospheric models. The procedure is discussed in Appendix A.

For the sky background subtraction, we note that in some spectra the terrestrial Na I D emission components (both natural and artificial) are not completely removed. Because of the wavelength shift of most features, this problem affects only a Galactic absorption close to null restframe velocity (see Sect. 3), whose profile (and thus equivalent width) is most likely affected by the incomplete sky subtraction.

Equivalent widths (EW) were estimated by integrating the line profiles in the telluric-corrected spectra. The local pseudo-continuum was derived by means of a straight line least-squares fit to two symmetric, equally extended regions on either side of the absorption. The EW uncertainty was derived using the formulation by Chalabaev & Maillard (1983), which includes the uncertainty on the continuum determination.

3. Narrow absorption features in SN 2011fe

3.1. Ca II *H&K and* Na I *D*

Several Ca II H, K and Na I D components are detected at different velocities, as shown in Fig. 1, which presents the highest resolution spectra available for the two wavelength ranges

(obtained with HERMES and SARG, respectively; see Tables 1 and 2).

Two main Galactic absorption systems are detected around −70 and −20 km s^{-1} (marked as A and B in Fig. 1), with weaker and diffuse absorptions possibly present at intermediate velocities (see the Ca II profile). A third system is clearly detected at about +130 km s^{-1} (C). The recession velocity of M101 is 241 ± 2 km s^{-1} (de Vaucouleurs et al. 1991), and therefore this component may be generated within a high-velocity cloud (HVC) that belongs either to the Milky Way or to the host galaxy. The radial velocity derived from 21-cm line observations at the projected SN site is about 180 km s^{-1} (Bosma et al. 1981; their Fig. 1). This makes the association to M101 more plausible, although not certain (see also Sect. 5). Finally, we detect an absorption system with two main components at about 180 and 195 km s^{-1} (D). These velocities are fully consistent with the radial velocity field at the projected SN location (Bosma et al. 1981). This strongly suggests that the corresponding absorptions arise in M101. All features are detected in both H and K lines, while system C is not detected in Na I. The component close to 195 km s^{-1} is clearly detected in Na I only in the highest signal-to-noise (S/N) spectrum (SARG, day 11) with a total equivalent width EW = 7 ± 2 mÅ, while it is only marginally detected in all other spectra.

Nugent et al. (2011c) reported the detection of one single absorption feature (EW = 45 ± 9 mÅ), which they identified as Na I D$_2$ at v = 194 ± 1 km s^{-1}. Although the weighted average EW we derive from our data (EW(Na I D_2) = 47 ± 1 mÅ, EW(Na I D$_1$) = 27 ± 1 mÅ; see Sect. 5.1) is consistent with that reported by Nugent et al., the velocity discrepancy is statistically very significant (∼14 km s^{-1}), and cannot be explained in terms of the quoted errors. Once applying the heliocentric corrections listed in Table 1 to the different spectra, the velocities deduced for the Na I D components all agree to within a few 0.1 km s^{-1}. The average heliocentric velocity deduced from the best-fit profile of the most intense host galaxy component (see Sect. 5) is 179.6 ± 0.2 km s^{-1}. Given the very consistent results we obtain from different setups and epochs, we consider our result to be correct to within the reported errors.

3.2. Other absorptions

A careful inspection of the telluric-corrected spectra that cover relevant wavelength range shows no trace of the two typical K I lines at 7665 and 7699 Åfor the Galaxy or for M101 (at the velocities derived for the Ca II and Na I features. See previous section). For the host galaxy the 5-σ detection limit derived from the HERMES spectrum taken on day 15 is EW(K I λ7699) < 5 mÅ. The K I λ7665 is severely affected by a telluric absorption, and so the upper limit estimate for this line is more problematic. However, the two lines have very similar strengths, and so the limit derived above applies to both of them. Similar considerations apply to the non-detection of Ti II, Ca I, CH and CH+. Finally, none of the known strong Diffuse Interstellar Bands (DIBs; 5780, 5797, 6284, 6379, 6613; Herbig 1995) are detected.

4. Reddening

The galactic Na I D components are very weak (see Fig. 1), indicating that SN 2011fe suffers a very low Galactic reddening. The integrated EW(Na I D$_1$) derived from our highest S/N spectrum (SARG, day 11) for the Galactic components (systems A and B in Fig. 1) is 38 ± 5 mÅ. Applying the relation inferred by Munari & Zwitter (1997) for Galactic reddening, we derive E_{B-V} = 0.01, which is consistent with the expected Galactic extinction along the line of sight to M 101 (E_{B-V} = 0.009 mag; Schlegel et al. 1998). According to the Munari & Zwitter relation, the expected EW for the K I λ7699 is ∼4 mÅ, which is fully consistent with the lack of K I detection in our spectra.

As shown in the previous section, we detect two features most probably associated to the host galaxy, at ∼180 and ∼200 km s^{-1}, with the latter contributing only marginally to the total Na I column density. The integrated D$_2$ EW measured on the SARG spectrum (day 11) is 47 ± 2 mÅ (EW(Na I D$_1$) = 25 ± 1 mÅ). Applying the Munari & Zwitter relation, this turns into E_{B-V} = 0.014 (A_V = 0.04 mag), in agreement with the value derived by Nugent et al. (2011c) using the same method. Because the total EW(Na I D$_2$) is 85 ± 6 mÅ, we conclude that the reddening along the line of sight to SN 2011fe is most probably lower than 0.05 (Munari & Zwitter 1997).

5. Narrow absorption line modeling

To derive interstellar cloud velocities, Doppler widths, and column densities we modeled the best resolution and S/N ratio spectra using the VAPID routine (Howarth et al. 2002). Saturation effects were implicitly taken into account by fitting simultaneously lines of the same species (Na I D$_1$ and D$_2$; Ca II H and K). The results for the FIES, HERMES and SARG (first epoch only) spectra are shown in Figs. 2 and 3 for Na I and Ca II. The Na I spectra require five components for a good fit, while nine components were required for Ca II. Error estimates were derived using Monte Carlo noise replication. The models were re-fitted to 1000 replicated data-sets, each with Gaussian noise of rms equal to that of the continuum added. The ±68% ranges in the resulting data give rigorous 1-sigma errors on each parameter. Table 3 shows the results for each epoch, as well as the results of a weighted-average fit to all epochs, in which the fitted data points were weighted by the continuum S/N ratio of the respective spectra. The data show no evidence for statistically significant variations in cloud component velocities or Doppler b parameters between epochs (see below), therefore the v and b values were held fixed at the weighted-average fit values and only the N values were allowed to vary for each epoch. Column densities (cm^{-2}) are given as base-ten logarithms. The units of v and b are km s^{-1}.

The analysis of Milky Way interstellar gas is beyond the scope of this paper. Here we mention that for the most pronounced Galactic feature (−23 km s^{-1}), the N(Na I)/N(Ca II) ratio is ∼0.50, which is typical of galactic halos (Hobbs 1978; Crawford 1992; Bertin et al. 1993). Sembach & Danks (1994) measured a mean Galactic halo N(Na I)/N(Ca II) ∼ 0.5.

Interestingly, the N(Na I)/N(Ca II) ratio for the main feature in M101 (+180 km s^{-1}) is ∼0.43, indicating that it may also originate in the halo of the host galaxy (see also King et al. 1995, for the case of SN 1994D). The really deviating case is that of the component at ∼128 km s^{-1}, which is clearly detected in Ca II, but not in Na I. The upper limit to the Na I column density deduced from the high S/N ratio SARG spectrum (day 11) is 1.5 × 10^{10} cm^{-2}, which yields N(Na I)/N(Ca II) ≤ 0.04. Such low values are rarely observed and indicate a mild depletion of calcium onto dust grains. A similar case was observed for one high-velocity component along the line of sight to SN 2000cx, where Ca II was detected, while Na I was not (Patat et al. 2007b). The corresponding ratio was N(Na I)/N(Ca II) ≤ 0.1.

Table 3. Na I and Ca II interstellar cloud model parameters.

Weighted average			Day 8	Day 11	Day 15	Day 21	Day 37
v	b	N	N	N	N	N	N
				Na I			
−67.2	2.1	$10.52^{+0.08}_{-0.11}$	$10.52^{+0.18}_{-0.26}$	$10.53^{+0.06}_{-0.07}$	$10.36^{+0.16}_{-0.19}$	$10.62^{+0.08}_{-0.10}$	$10.50^{+0.18}_{-0.25}$
−23.3	3.0	$10.74^{+0.07}_{-0.08}$	$10.70^{+0.13}_{-0.16}$	$10.80^{+0.04}_{-0.04}$	$10.80^{+0.07}_{-0.08}$	$10.73^{+0.06}_{-0.08}$	$10.60^{+0.16}_{-0.20}$
−12.6	3.4	$10.55^{+0.11}_{-0.11}$	$10.18^{+0.35}_{-0.79}$	$10.64^{+0.06}_{-0.06}$	$10.27^{+0.20}_{-0.29}$	$10.66^{+0.08}_{-0.09}$	$10.80^{+0.11}_{-0.14}$
179.6	3.8	$11.44^{+0.02}_{-0.02}$	$11.43^{+0.03}_{-0.04}$	$11.43^{+0.01}_{-0.01}$	$11.43^{+0.02}_{-0.02}$	$11.44^{+0.02}_{-0.02}$	$11.51^{+0.03}_{-0.03}$
193.6	6.4	$10.57^{+0.12}_{-0.16}$	$10.56^{+0.20}_{-0.29}$	$10.46^{+0.09}_{-0.13}$	$10.50^{+0.16}_{-0.18}$	$10.64^{+0.11}_{-0.11}$	$10.42^{+0.26}_{-0.46}$
				Ca II			
−66.4	0.7	$11.10^{+0.17}_{-0.20}$	$11.05^{+0.34}_{-0.69}$		$11.15^{+0.16}_{-0.21}$	$11.07^{+0.18}_{-0.24}$	
−65.7	32.0	$11.90^{+0.07}_{-0.07}$	$12.00^{+0.08}_{-0.07}$		$11.85^{+0.10}_{-0.10}$	$11.89^{+0.09}_{-0.10}$	
−37.5	1.0	$10.91^{+0.20}_{-0.24}$	<11.10		$10.91^{+0.20}_{-0.30}$	$10.97^{+0.18}_{-0.25}$	
−23.5	3.1	$11.04^{+0.17}_{-0.24}$	$11.00^{+0.23}_{-0.35}$		$11.03^{+0.19}_{-0.26}$	$11.03^{+0.17}_{-0.26}$	
−9.4	7.3	$11.63^{+0.06}_{-0.06}$	$11.72^{+0.07}_{-0.09}$		$11.61^{+0.08}_{-0.08}$	$11.58^{+0.08}_{-0.10}$	
127.8	6.2	$11.54^{+0.07}_{-0.07}$	$11.61^{+0.09}_{-0.10}$		$11.55^{+0.07}_{-0.10}$	$11.46^{+0.09}_{-0.13}$	
179.2	5.5	$11.82^{+0.04}_{-0.04}$	$11.89^{+0.05}_{-0.07}$		$11.80^{+0.05}_{-0.06}$	$11.78^{+0.05}_{-0.05}$	
197.0	6.7	$11.58^{+0.07}_{-0.08}$	$11.64^{+0.08}_{-0.09}$		$11.50^{+0.09}_{-0.11}$	$11.60^{+0.09}_{-0.09}$	
218.5	3.5	$10.89^{+0.21}_{-0.31}$	<11.10		$10.99^{+0.18}_{-0.31}$	$10.82^{+0.26}_{-0.50}$	

Finally, King et al. (1995) found N(Na I)/N(Ca II) = 0.1–0.3 for the high-velocity clouds observed along the line of sight to SN 1994D. Low ratios are, in general, typical of high velocity gas (Siluk & Silk 1974). The low value we derived for the component at ∼180 km s^{-1} is similar to those observed in intermediate- and high-velocity clouds by Molaro et al. (1993), who concluded that these clouds may contain very little dust, with calcium and sodium mainly in gaseous form (see also the properties measured by Cox et al. 2007, toward the LMC sight-lines). For these reasons it is reasonable to conclude that absorption system C (see Fig. 1) arises in an HVC.

5.1. Time evolution

The derived cloud parameters show some marginal evidence for time variability. The only possibly significant variation is seen for the host galaxy Na I component at ∼180 km s^{-1}. While the logarithmic column density derived for this absorption is 11.44 ± 0.02 on days 8, 11, 15 and 21, on day 37 this grows to 11.52 ± 0.03, which indicates a variation at the 3-sigma level. One may be tempted to attribute this fluctuation to the different instrumental setups. However, a direct comparison of the two spectra taken on days 8 and 37 (both obtained with FIES and the same setup) clearly shows that both components D_1 and D_2 had consistently deepened by about 16% on the second epoch, while their FWHM remained unchanged. The integrated EWs directly measured on the two spectra are 23.6 ± 1.9, 46.1 ± 2.0 mÅ, and 30.4 ± 2.4, 53.0 ± 2.5 mÅ for D_1 and D_2 on the two epochs, respectively, implying a variation ΔEW(Na I D_2) = 6.9 ± 3.2 mÅ. This strengthens the conclusion that whatever the reason for the change it cannot be attributed to a variation of instrumental resolution[3].

Although AES spectra have a significantly lower resolution (16.7 km s^{-1}, see Table 2), given the simple structure of the component at ∼180 km s^{-1}, they can be used together with the higher resolution data to study the variability on the whole time range spanned by the available observations (the relevant spectral regions are presented in Fig. A.2). To increase the S/N ratio we stacked the last two AES epochs (days 84 and 86).

In Table 4 we report the EWs of Na I D_2 and D_1 directly measured on all our spectra, together with their associated rms uncertainties, the S/N ratio achieved at 5900 Å, and the FWHM resolution. The weighted average EWs computed over all epochs for the two lines are 47.1 ± 0.8 mÅ and 27.4 ± 1.1 mÅ, respectively (the standard deviation of the EW measurements is 2.6 and 3.4 mÅ, respectively). The EWs are plotted as a function of time in Fig. 4 (empty symbols indicate the lower resolution AES data). Although all measurements are within less than 3-sigma from the weighted average (and are therefore formally consistent with a null variation), there is a systematic increase in both components. This becomes more evident if one considers only the higher resolution data (filled symbols in Fig. 4). However, the overall trend is mainly dominated by the last SARG measurement, which is characterized by a low S/N ratio, and may therefore be affected by larger systematic errors (e.g. continuum determination and telluric correction). For this reason, we do not attach too much confidence to it.

Because of the measured standard deviation (see above), the expected ±3-σ peak-to-peak range is 2 × 3 × 2.6 mÅ = 15.6 mÅ. Considering the two extreme values (days 15.1 and 86.4), the observed peak-to-peak Na I D_2 EW variation amounts to 15.6 ± 6.5 mÅ. This is fully consistent with the expected value, and we therefore regard it as an upper limit on the observed EW variation. This is very small compared to the changes seen in SN 2006X (Patat et al. 2007a), and SN 2007le (Simon et al. 2009) during the first three months of their evolution, which exceeded 100 mÅ[4].

The fast SN expansion, coupled to the patchy nature of the ISM, can produce short time-scale changes in the IS absorption

[3] Because it is a fiber-fed spectrograph, FIES is not subject to changes of resolution caused by seeing variations. Moreover, a check on the comparison lamp emission lines on the two epochs shows that the resolution indeed remained constant.

[4] Even stronger variations were reported for SN 1999cl (Blondin et al. 2009) and SN 2006dd (Stritzinger et al. 2010), but no high-resolution spectroscopy was available in those cases.

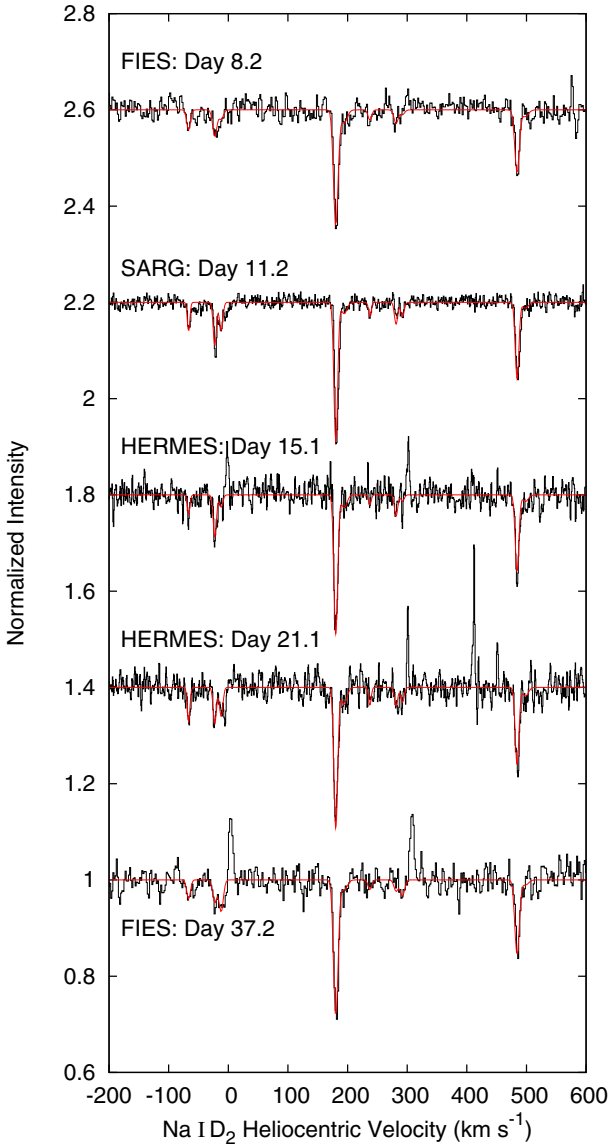

Fig. 2. Na I D spectra for each epoch (black histograms), with best-fit models overlaid (red curves). Spectra were normalized and offset vertically for display. Heliocentric velocity scale is given with respect to the Na D$_2$ line rest wavelength. The spurious emissions observed in some spectra around 0 and 300 km s^{-1} are residuals of the sky subtraction (see Sect. 2).

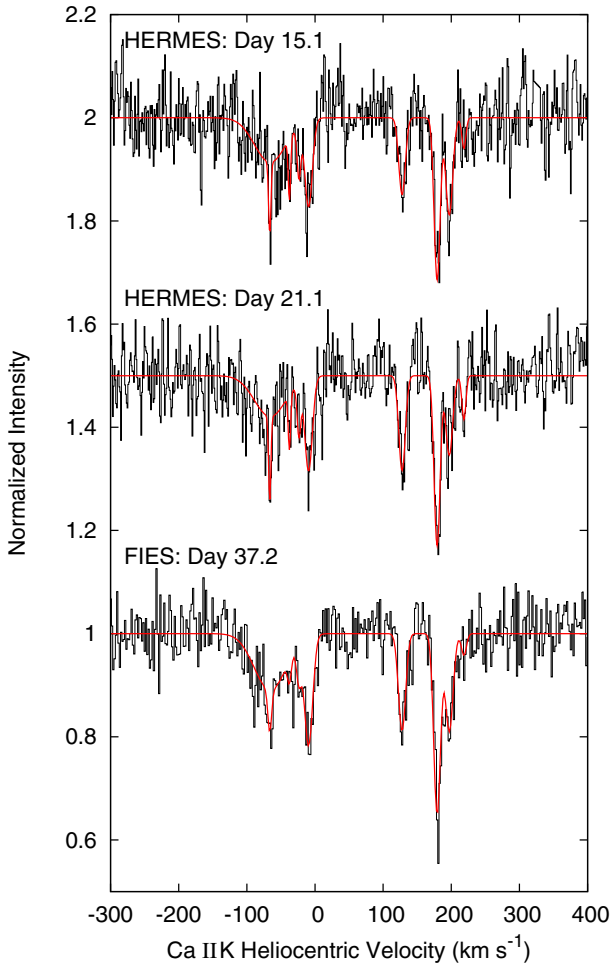

Fig. 3. Ca II K spectra for each epoch for which these data were obtained (black histograms), with best-fit models overlaid (red curves). Spectra were normalized and offset vertically for display. Heliocentric velocity scale is given with respect to the Ca II K line rest wavelength.

features. The analysis of their variations can be used to study the ISM small scale structure down to a few tens of AUs (Patat et al. 2010). The data currently available for SN 2011fe allow us to apply this method for the first three months of the SN evolution, when the photospheric radius increased from ∼10 AU to ∼350 AU. The simulations, run along the lines described in Patat et al. (2010), show that peak-to-peak variations $\Delta EW \lesssim 15$ mÅ imply $\Delta N \lesssim 4 \times 10^{11}$ cm^{-2} ($\Delta N/N \lesssim 1.4$). The maximum deviation measured in our simulations between any pair of epochs in the simulated data-set is ∼16 mÅ. The rms EW variation from the weighted average is 2.6 mÅ, matching the value derived from the data (see previous section).

The derived density contrast is compatible with the values measured in the Milky Way (Frail et al. 1994) and, therefore, the upper limit on the column density variation is fully in line with what is expected for a diffuse ISM with the same properties as in our own Galaxy. In other words, even if the observed fluctuations were real (including the apparent steady growth), these are consistent with the geometrical effect described in Patat et al. (2010). Therefore, we conclude that the absorption feature observed at ∼180 km s^{-1} is most likely associated to the ISM, and is placed at distances larger than ∼10^{19} cm (∼10 light years) from the explosion site, where the effects of the SN radiation field on the Na I ionization balance are negligible (Patat et al. 2007a; Simon et al. 2009). Unfortunately, the S/N ratio at ∼3900 Å in our data is not sufficient to study with the required accuracy the evolution of the Ca II H&K features, which in SNe 2006X and 2007le showed a distinct behavior (Patat et al. 2007a; Simon et al. 2009).

6. Discussion and conclusions

SN 2011fe is a slightly subluminous, Branch-normal explosion, very similar to the well studied SN 1994D (Nugent et al. 2011c). However, it is by no means clear whether all "normal" events, which share very similar spectroscopic and photometric properties, do also share a common progenitor channel. For this reason it is important to tie the reasonably well known progenitor nature of this particular event to other properties, which may allow us to identify similar events in less favorable cases, i.e. at

Table 4. Na I D equivalent widths.

Setup	Epoch (days)	$EW(D_2)$ (mÅ)	$EW(D_1)$ (mÅ)	S/N (5900 Å)	Resolution (km s^{-1})
*	1.5	45.0 ± 9.0	–	–	6.0
FIES#1	8.2	46.1 ± 2.0	23.6 ± 1.9	60	6.3
SARG#1	11.2	46.6 ± 1.5	26.3 ± 1.0	115	4.5
HERMES#1	15.1	44.3 ± 1.8	27.6 ± 1.8	50	3.7
AES#1	21.1	49.2 ± 2.2	34.2 ± 1.9	130	16.7
HERMES#2	21.1	44.3 ± 1.8	27.6 ± 1.8	50	3.7
AES#2	22.1	53.8 ± 4.2	28.5 ± 4.0	105	16.7
AES#3	29.1	51.9 ± 2.7	31.0 ± 2.2	190	16.7
AES#4	30.1	44.5 ± 2.3	33.7 ± 2.5	155	16.7
FIES#2	37.2	53.0 ± 2.5	30.4 ± 2.4	55	6.3
AES#5	56.1	48.7 ± 7.1	34.4 ± 7.3	50	16.7
AES#6+#7	85.2	58.7 ± 3.7	33.5 ± 3.0	115	16.7
SARG#2	86.4	59.9 ± 6.2	23.7 ± 7.3	16	4.5
Weighted average		47.1 ± 0.8	27.4 ± 1.1		

Notes. (*) The first epoch is from Nugent et al. (2011c).

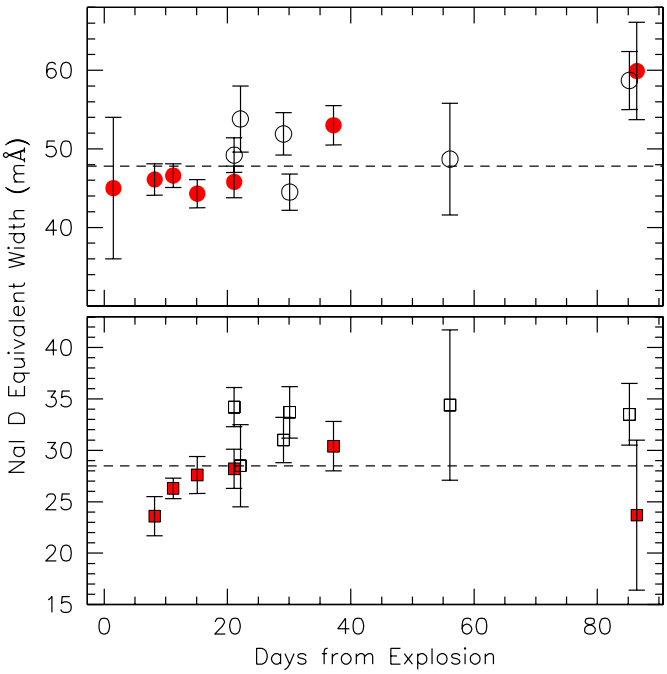

Fig. 4. EW time evolution of Na I D_2 (*upper panel*) and D_1 (*lower panel*). Values are from Table 4. The short-dashed horizontal lines mark the weighted average values. AES data are identified by empty symbols.

larger distances and without such exceptionally early discoveries. Among these is the circumstellar environment.

The method proposed by Patat et al. (2007a) that was subsequently expanded by Simon et al. (2009) has been applied to study the CSM of number of SNe Ia. In two cases it led to the detection of time-variant Na I features, which were interpreted as arising in the material lost by the progenitor system before the explosion (Patat et al. 2007a; Simon et al. 2009). The velocities of this material are consistent with those of a red giant, hence favoring a symbiotic system. The complex velocity structure shown by SN 2006X was explained as being the possible outcome of recurrent-novae episodes (Patat et al. 2007a). This suggestion is supported by the results of a similar analysis carried out on the known recurrent nova RS Oph, which shows strikingly similar CSM properties (Patat et al. 2011).

A study conducted on a large number of SN Ia has shown a statistically significant excess of blueshifted Na I features, which were interpreted as arising in material lost by the progenitor system (Sternberg et al. 2011). In addition, Foley et al. (2012) found that SN Ia displaying blue-shifted absorption features are characterized by higher ejecta velocities and redder colors with respect to the rest of the SN Ia sample. This gives support to the conclusions reached for SNe 2006X and 2007le. If this interpretation is correct, the measured fraction of SN Ia that display blueshifted features indicates that this channel is not a significant contributor to the global rate of thermonuclear events.

This result has to be reconciled with opposing evidence provided by the lack of CSM signatures in radio, UV, and X-ray domains. The two apparently contradicting results may be reconciled by a complex CSM structure (Patat 2011, Chomiuk et al. 2011), a delay between mass loss and SN explosion (Chomiuk et al. 2012; Margutti et al. 2012), or stellar evolution effects (Justham 2011). In this context we emphasize that, although it showed a marked Na I variation, SN 2006X was not detected by the VLA (Stockdale et al. 2006; Chandra, et al. 2006). Therefore, if the interpretation of the blueshifted absorption features is correct, the absence of a radio detection does not necessarily imply that the CS environment is "clean".

What makes SN 2011fe special is that its progenitor system was constrained with a significant confidence through a number of very stringent constraints (Li et al. 2011; Brown et al. 2012; Nugent et al. 2011c; Bloom et al. 2011; Liu et al. 2012). The absence of time-variable, blueshifted features and the "clean" environment reported in this paper fully agrees with the progenitor nature derived from the very early observations. The key question is whether the argument can be reversed, and the absence of such features in any SN Ia can be interpreted in terms of a similar progenitor, at least in a statistical sense. The answer to this question is awaiting detailed hydrodynamical modeling, which would tell us how frequently the physical conditions for producing observable narrow features are met, and what the viewing angle effects are (Mohamed et al., in prep.). Before this is accomplished, we can only speculate based on very small numbers.

As pointed out by Nugent et al. (2011c), SN 2011fe is spectroscopically very similar to the somewhat subluminous events SN 1992A (Kirshner et al. 1993) and SN 1994D (Patat et al. 1996). Although the link between these objects needs to be assessed considering a number of observables, we notice that all three objects present a very "clean" circum/interstellar environment (Kirshner et al. 1993; King et al. 1995; Patat et al. 1996). In the schema devised by Sternberg et al. (2011), SNe 1994D and 2011fe would be classified in the single/symmetric group (SS-type, 14.3%), while SN 1992A would fall in the group with no absorption detection (N-type, 37.1%). An inspection of the SS group shows that three SS-type events (out of five) have a single component, similar to SN 2011fe. If we assume that in all these cases the absorption is attributable to the host galaxy (and not to the CSM environment), and we add them to the N-type events, then the fraction of "clean" events in the Sternberg et al. sample is ∼46%. One can imagine cases where the CSM environment is "clean", but the line of sight intercepts ISM clouds that are totally unrelated to the progenitor. Therefore, while the lack of conspicuous absorption features can be confidently interpreted in terms of a gas-free environment, the reverse argument does not hold.

The projected position of SN 2011fe falls close to a peripheral spiral arm (see for instance Nugent et al. 2011c). However,

the very low reddening and the absence of complex absorption structures strongly suggest that the explosion took place on the front side of the face-on host, most probably well above its galactic plane. Had the SN been placed on the rear side of the galaxy, the IS imprints would have been much more complex, irrespective of the progenitor's nature deduced from the early data. Therefore the above fraction can only represent a lower limit. On the other hand, because of the viewing angle effects, the fraction of events allegedly produced by systems that host a giant estimated by Sternberg et al. (2011) is also a lower limit (20–25%).

The sample of SN Ia with sufficient spectral resolution and time coverage is still relatively small, and therefore it may be premature to draw conclusions. The fraction of events showing time-variant features is ~17% (Patat 2011). Probing only the line of sight, this indicator also suffers from viewing-angle effects. In addition, the method only reveals material placed in the suitable range of distances from the SN that has the required densities (Patat et al. 2007a; Simon et al. 2009). Therefore, again, it gives only a lower limit to the fraction of events generated through this channel. Interestingly, this limit is reasonably similar to that derived from the excess of blue-shifted features (20%; Sternberg et al. 2011), and it supports the conclusion that this channel contributes in a significant way to the global SN Ia rate.

Acknowledgements. This work has been conducted in the framework of the European collaboration SN Variety and Nucleosynthesis Yields. This work is partially based on observations made with the Mercator Telescope, operated on the island of La Palma by the Flemish Community, at the Spanish Observatorio del Roque de los Muchachos of the Instituto de Astrofísica de Canarias. This work is partially based on observations obtained with the HERMES spectrograph, which is supported by the Fund for Scientific Research of Flanders (FWO), Belgium, the Research Council of K. U. Leuven, Belgium, the Fonds National Recherches Scientific (FNRS), Belgium, the Royal Observatory of Belgium, the Observatoire de Geneve, Switzerland and the Thüringer Landessternwarte Tautenburg, Germany. This work is partially based on observations made with the Nordic Optical Telescope, operated on the island of La Palma jointly by Denmark, Finland, Iceland, Norway, and Sweden, in the Spanish Observatorio del Roque de los Muchachos of the Instituto de Astrofisica de Canarias. This work is partially based on observations made with the SARG spectrograph at the Italian Telescopio Nazionale Galileo (TNG), operated on the island of La Palma by the Fundaciòn Galileo Galilei of the INAF (Istituto Nazionale di Astrofisica) at the Spanish Observatorio del Roque de los Muchachos of the Instituto de Astrofisica de Canarias. This work is partially based on data collected at the 1.82 m Copernico telescope on Mt. Ekar (Asiago, Italy). M.C. thanks the NASA Astrobiology Institute via the Goddard Center for Astrobiology. V.S. acknowledges financial support from Fundação para a Ciência e a Tecnologia under program Ciência 2008 and a research grant PTDC/CTE-AST/112582/2009.

Appendix A: Removal of telluric features

Although the spectral region of Ca II H&K is free of telluric absorption features, this is not the case for Na I D, and especially K I λ7665 and λ7699. Because the observations were conducted mostly at relatively high airmasses (see Table 1), these are quite severely disturbed by water bands.

The removal of telluric absorption features is usually performed using spectra of bright stars obtained with the same instrumental setup and similar airmass as for the scientific target. In this paper we adopted a different approach, using an atmospheric transmission model (see for instance Stevenson 1994; Seifahrt et al. 2010). The advantages over a direct observation are a) the absence of intrinsic photospheric features; b) the absence of interstellar features (chiefly Na I D lines); c) the infinite S/N ratio, and d) the exact wavelength scale. The latter provides an absolute reference to which the observed spectra can be corrected via cross-correlation techniques (see below).

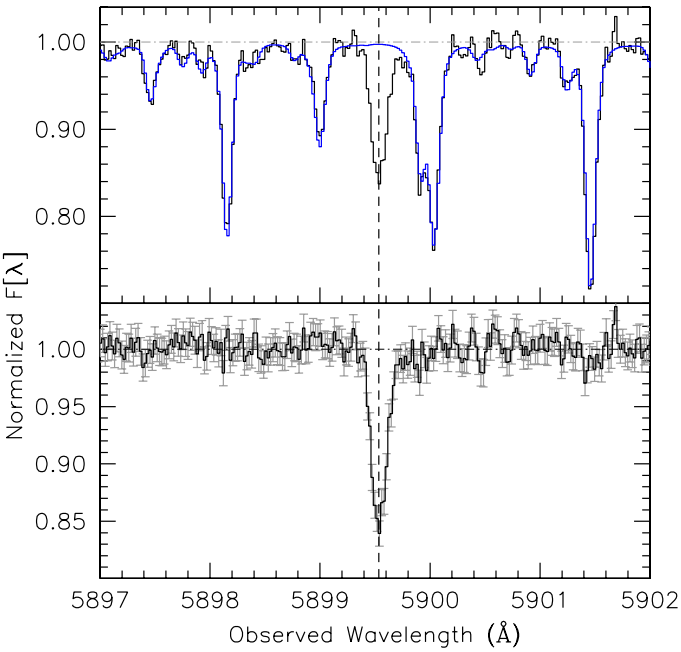

Fig. A.1. Example of telluric features removal for the SARG spectrum in the region of Na I D_1. *Upper panel*: observed data (black line) and best fit LBLRTM model (blue line). *Lower panel*: telluric-corrected spectrum. The dashed vertical line marks the position of Na I D_1 (v_{hel} ~180 km s^{-1}). The S/N ratio on the continuum is about 100 (the error-bars indicate the estimated rms noise).

In this work we adopted the Line By Line Radiation Transfer Model (LBLRTM; Clough et al. 2005). This code is based on the HITRAN database (Rothman et al. 2009). It has been validated against real spectra from the UV to the sub-millimeter, and is widely used for the retrieval of atmospheric constituents[5]. LBLRTM solves the radiative transfer using an input atmospheric profile, which contains the height profiles for temperature, pressure, and chemical composition. For our purposes we adopted the standard LBLRTM equatorial profile.

After computing the synthetic model in the regions of interest and for the given airmass, this is convolved with the instrumental profile and the wavelength correction is computed via cross-correlation. The absence of intrinsic narrow absorptions in the SN spectrum and the weakness of the interstellar features in the Na I and K I regions (see below) make the correlation function peak very well defined. The wavelength solutions for FIES, HERMES and SARG spectra were all found to match the model wavelength with a maximum deviation of 130 m s^{-1}, that is more than five times smaller than the pixel size. Therefore, no wavelength correction was applied to these data. For the AES spectra, maximum deviations of 6.6 km s^{-1} (about one pixel) were found, and the spectra were corrected accordingly. The final wavelength accuracy is ~0.1 km s^{-1} for the FIES, HERMES and SARG data, while it is ~0.3 km s^{-1} for the AES spectra.

An example of telluric correction is presented in Fig. A.1 for the SARG spectrum. All telluric features are removed at the level of a few percent, which is comparable to (or better than) the continuum rms noise of all spectra presented in this paper.

[5] See http://rtweb.aer.com/lblrtm.html

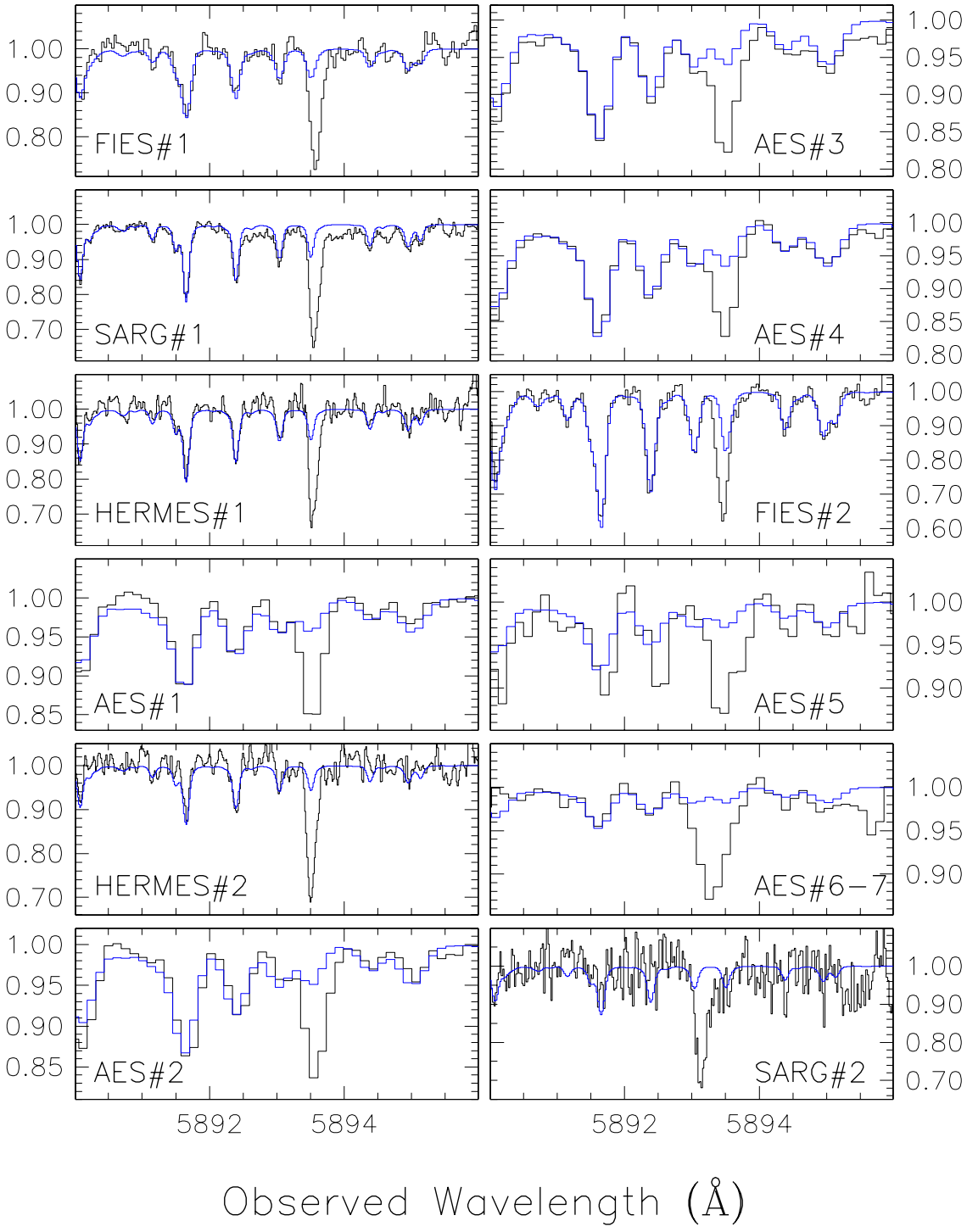

Fig. A.2. Region of the Na I D_2 at the host galaxy restframe velocity for the twelve epochs presented in this paper. The blue curves trace the best-fit telluric synthetic spectrum.

The best-fit telluric spectra for all epochs are presented in Fig. A.2 for the Na I region at the host galaxy restframe velocity.

References

Bertin, P., Lallement, R., Ferlet, R., & Vidal-Madjar, A. 1993, A&A, 278, 549
Bianco, F. B., Howell, D. A., Sullivan, M., et al. 2011, ApJ, 741, 20
Blondin, S., Prieto, J. L., Patat, F., et al. 2009, ApJ, 693, 207
Bloom, J. S., Kasen, D., Shen, K. J., et al., 2012, ApJ, 744, L17
Bosma, A., Goss, W. M., & Allen, R. J. 1981, A&A, 93, 106
Brown, P. J., Dawson, K. S., de Pasquale, M., et al. 2012, ApJ, 753, 22
Chalabaev, A., & Millard, J. P. 1983, A&A, 127, 279
Chandra, P., Chevalier, R., & Patat, F. 2006, ATel, 954
Chomiuk, L., Soderberg, A. M., Chevalier, R., Badenes, C., & Fransson, C. 2011, A&AS, 21730405C
Chomiuk, L., Soderberg, A. M., & Moe, M. 2012, ApJ, 750, 164
Clough, S. A., Shephard, M. W., Mlawer, E. K., et al. 2005, J. Quant. Spectrosc. Radiat. Transfer, 91, 233
Cox, N. L. J., & Patat, F. 2008, A&A, 485, L9
Cox, N. L. J., Cordiner, M. A., Ehrenfreund, P., et al. 2007, A&A, 470, 941
Crawford, I. A. 1992, MNRAS, 254, 264
de Vaucouleurs, G., de Vaucouleurs, A., Corwin, H. G., et al. 1991, Third Reference Catalogue of Bright Galaxies, Ver. 3.9
Deshpande, A. A. 2000, MNRAS, 317, 199

Foley, R. J., Simon, J. D., Burns, C. R., et al. 2012, ApJ, 752, 101
Frail, D. A., Weisberg, J. M., Cordes, H. M., & Mathers, A. 1994, ApJ, 436, 144
Gratton, R. G., Bonanno, G., Bruno, P., et al. 2001, Exp. Astron., 12, 107
Hayden, B. T.,Garnavich, P. M., & Kasen, D. 2010, ApJ, 722, 1691
Heiles, C. 1997, ApJ, 481, 193
Herbig, G. H. 1995, ARA&A, 33, 19
Hobbs, L. M. 1978, ApJS, 38, 129
Horesh, A., Kulkarni, S. R., Fox, D. B., et al. 2012, ApJ, 746, 21
Horne, K. 1986, PASP, 98, 609
Howarth, I. D., Price, R. J., Crawford, I. A., & Hawkins, I. 2002, MNRAS, 335, 267
Immler, S. I., Brown, P. J., Milne, P., et al. 2006, ApJ, 648, L119
Justham, S. 2011, ApJ, 730, L34
King, D. L., Vladilo, G., Lipman, K., et al. 1995, A&A, 300, 881
Kirshner, R. P., Jeffery, D. J., Leibundgut, B., et al. 1993, ApJ, 415, 589
Leonard, D. C. 2007, ApJ, 670, 1275
Li, W., Bloom, J. S., Podsiadlowski, Ph., et al. 2011, Nature, 480, 348
Liu, J., Di Stefano, R., Wang, T., & Moe, M. 2012, ApJ, 749, L141
Lundqvist, P., Sollerman, J., Leibundgut, B., et al. 2003, in From twilight to highlight: the physics of Supernovae, eds. W. Hillebrandt, & B. Leibundgut (Berlin: Springer), 309
Lundqvist, P., Matheson, T., Sollerman, J., et al. 2005, in Cosmic Explosions, eds. J. M. Marcaide, & K. W. Weiler, CD-ROM version, IAU Coll., 192, 81
Margutti, R., Soderberg, A. M., Chomiuk, L., et al. 2012, ApJ, 751, 734
Mattila, S., Lundqvist, P., Sollerman, J., et al. 2005, A&A, 443, 649
Molaro, P., Vladilo, G., Monai, S., et al. 1993, A&A, 274, 505
Munari, U., & Zwitter, U. 1997, A&A, 318, 269
Nugent, P., Sullivan, M., Bersier, D., et al. 2011a, ATel #3581
Nugent, P., Magill, L., Kotak, R., et al. 2011b, CBET, 2791, 1
Nugent, P. E., Sullivan, M., Cenko, S. B., et al. 2011c, Nature, 480, 344
Panagia, N., Romaniello, M., Gilmozzi, R., et al. 2006, ApJ, 469, 396
Patat, F., 2011, in Binary paths to Type Ia Supernova explosions, IAUS. 281, AIPC, eds. R. Di Stefano, & M. Orio, in press [arXiv:1109.5799]
Patat, F., Benetti, S., Cappellaro, E., et al. 1996, MNRAS, 278, 111
Patat, F., Kumar, R., Barley, M. E., et al. 2007a, Science, 30, 490
Patat, F., Jeffery, D. J., Leibundgut, B., et al. 2007b, A&A, 474, 931
Patat, F., Cox, N. L. J., Parrent, J., & Branch, D. 2010, A&A, 514, A78
Patat, F., Chugai, N. N., Podsiadlowski, Ph., et al. 2011, A&A, 530, A63
Raskin, G., van Winckel, H., Hensberge, H., et al. 2011, A&A, 526A, A69
Schlegel, D. J., Finkbeiner, D. P., & Davis, M. 1998, ApJ, 500, 525
Röpke, F. K., Kromer, M., Seitenzahl, I. R., et al. 2012, ApJ, 750, 19
Rothman, L. S., Gordon, I. E., Barbe, A., et al. 2009, J. Quant. Spectrosc. Radiat. Transfer, 110, 533
Seifahrt, A., Käufl, H. U., Zängl, G., et al. 2010, A&A, 524A, 11
Sembach, K. R., & Danks, A. C. 1994, A&A, 289, 539
Siluk, R. S., & Silk, J. 1974, ApJ, 192, 51
Simon, J., Gal-Yam, A., Gnat, O., et al. 2009, ApJ, 702, 1157
Sternberg, A., Gal-Yam, A., Simon, J. D., et al. 2011, Science, 333, 856
Stevenson, C. C. 1994, MNRAS, 267, 904
Stockdale, C. J., Kelley, M., Sramek, R. A., et al. 2006, CBET 396
Stritzinger, M., Burns, C. R., Phillips, M. M., et al. 2010, AJ, 140, 2036
Whelan, J., & Iben, I. 1973, ApJ, 186, 1007